Research articles

Tuning magnetic and structural properties of $MnFe_2O_4$ nanostructures by systematic introduction of transition metal ions M^{2+} (M = Zn, Fe, Ni, Co)

Fernando Arteaga-Cardona[a,*], Umapada Pal[a], José María Alonso[b,c], Patricia de la Presa[b,c], María-Eugenia Mendoza-Álvarez[a], Ulises Salazar-Kuri[a], Miguel Á. Méndez-Rojas[d]

[a] *Instituto de Física, Benemérita Universidad Autónoma de Puebla, Apdo. Postal J-48, Puebla, Pue 72570, Mexico*
[b] *Instituto de Magnetismo Aplicado, UCM-ADIF-CSIC, Las Rozas, Spain*
[c] *Departamento de Física de Materiales, UCM, Ciudad Universitaria, Madrid, Spain*
[d] *Departamento de Ciencias Químico-Biológicas, Universidad de las Américas Puebla, ExHda. Sta. Catarina Martir s/n, San Andrés Cholula, 72810 Puebla, Mexico*

ARTICLE INFO

ABSTRACT

Manganese ion (Mn^{2+}) in a ferrite nanostructure was partially substituted by different transition metal ions: Zn^{2+}, Fe^{2+}, Ni^{2+}, and Co^{2+}, in that respective order. The introduction of each different metal ion affected the size, the crystallographic parameters, and the magnetic properties of the ferrite nanoparticles. The magnetic properties changed accordingly with the individual characteristics of the selected transition metal ion, meaning that the introduction of a metal ion with lower coercivity like nickel or iron into the structure decreased the overall coercivity of the material; this also had an effect on increasing/decreasing the blocking temperature of the overall material. There were some unexpected variations at the crystalline structure and in its thermal stability, as demonstrated by X-ray diffraction, rietveld analysis, and TGA-DSC measurements. These changes can be attributed to lattice distortions caused by the substitution of different transition metal ions in the spinel structure, which affects its stability.

1. Introduction

Lodestone, a mineral rich in magnetite (Fe_3O_4), was one of the first magnetic materials known to humanity. The Greek philosopher Thales of Miletus first described it around the 6th century BCE and it was known also by ancient cultures such as Chinese and Olmecs, which used them as a directional device [1]. Since then, several ferrites (MFe_2O_4, M = Mn^{2+}, Fe^{2+}, Ni^{2+}, Co^{2+}, etc.) have been prepared by different synthetic routes like co-precipitation, thermal decomposition, micro-emulsion, etc. [2–4] and extensively studied for their technological applications in the fields of electronics (memory devices, inductors, high-frequency materials, power conversion, data storage, sensors) and biosciences (contrast agents, biomolecule separation and purification, drug delivery systems) [5–10].

The magnetic properties of ferrites can be explained by using the superexchange model, proposed in 1934 by Hendrik Kramers, and refined by Phillip Anderson in 1950. Later, in the 1950s, Goodenough and Kanamori [8] developed a set of semi-empirical rules for the superexchange. The superexchange phenomenon is described as an anti-ferromagnetic coupling between metal ions due to the presence of an atom with a complete electronic shell. In the case of ferrites, the diamagnetic nature of oxygen atoms is responsible for superexchange conformation. As the crystalline lattices of metal ferrites contain metal ions of two different oxidation states (M^{2+} and M^{3+}) with different Bohr magneton values, the final accommodation by applying the superexchange theory results in a net magnetization oriented in one axis, i.e. a ferrimagnetic material [11]. Considering that the magnetic superexchange interaction occurs between the M^{2+} and Fe^{3+} ions, the magnetic properties of metal ferrites can be tuned by changing the M^{2+} ions; increasing or decreasing their magnetic saturation, coercivity (H_c), and remanent magnetization (M_r). In addition, the blocking temperature (T_B) of metal ferrite nanostructures can also be tuned by varying the M^{2+} ion species.

The physical properties (optical, magnetic, electric, etc) of ferrites containing only one type of M^{2+} ion have been extensively studied and reported in the literature [12–17]. Partial substitution of M^{2+} ions in the host ferrite lattice with a different transition metal ion (M^{2+}), and even substituting the Fe^{3+} ion with rare earth ions (RE^{3+}) like Y^{3+} or Nd^{3+} [18–20] have also been investigated as a pathway for tailoring the magnetic and electric properties of ferrites, revealing excellent results for the design of a magnetic material for specific technological applications [7,21–23]. Nevertheless, to the best of our knowledge,

---

systematic incorporation of three (M''^{2+}), four (M'''^{2+}), or five (M''''^{2+}) different ions into a crystal lattice and its effect on the structural stability and magnetic properties of metal ferrite has not been performed so far. The inclusion of multiple divalent metal ions (M^{2+}) can lead new ways of tailoring the magnetic properties of metal ferrites through the alteration of superexchange coupling between Fe^{3+} and M^{2+} ions of different types, along with the distortion of ferrite lattice derived from the compensation effects produced by the substitution of atoms.

In this work, we report a study on the variations in the magnetic and crystallographic properties of ferrites due to the incorporation multiple M^{2+} ions in the spinel structure, taking the manganese ferrite ($MnFe_2O_4$) as a model host because it is a material with many potential applications such as transformers, MRI contrast agents, catalysis and supercapacitors among others, these promising applications are due to the low coercivity and high magnetic saturation, along with its low toxicity risk in comparison to other ferrites [2].

2. Materials and methods

Manganese (II) chloride tetrahydrate ($MnCl_2 \cdot 4H_2O$, > 98%), zinc chloride ($ZnCl_2$, > 98%), sodium hydroxide (NaOH, > 97%), iron (II) chloride tetrahydrate ($FeCl_2 \cdot 4H_2O$, > 98%), iron (III) chloride hexahydrate ($FeCl_3 \cdot 6H_2O$, > 97%), nickel (II) chloride hexahydrate ($NiCl_2 \cdot 6H_2O$, > 98%), cobalt (II) chloride hexahydrate ($CoCl_2 \cdot 6H_2O$, > 97%), iron (III) nitrate nonahydrate ($Fe(NO_3)_3 \cdot 9H_2O$, > 98%), hydrochloric acid (HCl, 37%) and nitric acid (HNO_3, 70%) of reagent grade were purchased from Sigma-Aldrich, Mexico, and used as received without further purification.

2.1. General synthesis

In general, for the preparation of magnetic ferrites of multiple metal mixed ions followed a coprecipitation route, mixing a solution containing the metal ions and an alkaline solution. The preparation for the aqueous solutions of the corresponding metal ion precursors are described in detail below. Briefly, the desired ion precursor solution was added to 50 mL of 2 M NaOH (pH 14) solution and stirred for 30 min at 100 °C. Finally, the obtained products were washed three times with deionized (DI) water to remove the excess of the precursor ions. A post-synthesis acid treatment was performed to all the produced ferrites to form their stable ferrofluids, minimizing the aggregation of the formed nanoparticles.

2.1.1. Ion precursor solution for manganese ferrite ($MnFe_2O_4$)
$MnFe_2O_4$ nanoparticles were prepared by adding 1 mL of a solution of $MnCl_2 \cdot 4H_2O$ (2.5 μmol) into a 5 mL solution of $FeCl_3 \cdot 6H_2O$ (5 μmol) in water.

2.1.2. Ion precursor solution for zinc-manganese ferrite ($Zn_{0.5}Mn_{0.5}Fe_2O_4$) (ZnMn)
For the synthesis of $Zn_{0.5}Mn_{0.5}Fe_2O_4$ (ZnMn) nanoparticles, 1 mL of $ZnCl_2$ (1.25 μmol) and 1 mL of $MnCl_2 \cdot 4H_2O$ (1.25 μmol) solutions were mixed with 5 mL of $FeCl_3 \cdot 6H_2O$ (5 μmol) solution.

2.1.3. Ion precursor solution for zinc-manganese-iron ferrite ($Zn_{0.4}Mn_{0.4}Fe_{2.2}O_4$) (ZnMnFe)
For the synthesis of ZnMnFe nanoparticles, a mixed metal precursor solution was prepared by mixing 1 mL of each of the $ZnCl_2$ (1 μmol), $MnCl_2 \cdot 4H_2O$ (1 μmol) and $FeCl_2 \cdot 4H_2O$ (0.5 μmol) solutions into a 5 mL of $FeCl_3 \cdot 6H_2O$ (5 μmol) solution.

2.1.4. Ion precursor solution for zinc-manganese-iron-nickel ferrite ($Zn_{0.3}Mn_{0.3}Ni_{0.2}Fe_{2.2}O_4$) (ZnMnFeNi)
For the preparation of ZnMnFeNi nanoparticles, a mixed metal precursor solution was prepared by mixing 1 mL of each of the $ZnCl_2$ (0.75 μmol), $MnCl_2 \cdot 4H_2O$ (0.75 μmol) and $FeCl_2 \cdot 4H_2O$ (0.5 μmol)

solutions into a 5 mL of $FeCl_3 \cdot 6H_2O$ (5 μmol) solution.

2.1.5. Ion precursor solution for zinc-manganese-iron-nickel-cobalt ferrite ($Zn_{0.2}Mn_{0.2}Ni_{0.2}Co_{0.2}Fe_{2.2}O_4$) (ZnMnFeNiCo)
For the preparation of ZnMnFeNiCo nanoparticles, a mixed metal precursor solution was prepared by mixing 1 mL of each of the $ZnCl_2$ (0.5 μmol), $MnCl_2 \cdot 4H_2O$ (0.5 μmol), $FeCl_2 \cdot 4H_2O$ (0.5 μmol), $NiCl_2 \cdot 6H_2O$ (0.5 μmol) and $CoCl_2 \cdot 6H_2O$ (0.5 μmol) solutions into 5 mL of $FeCl_3 \cdot 6H_2O$ (5 μmol) solution.

2.2. Stabilization of the aqueous nanoparticle suspensions

Stabilization of the synthesized nanoparticles in aqueous suspensions was achieved by acid peptization in water to reduce their aggregation potential. Briefly, 15 mL of HNO_3 (2 M) was added to the obtained black precipitates and the resulting mixture was stirred for 15 min. After that, the supernatant was magnetically decanted and 25 mL of a 1 M $Fe(NO_3)_3 \cdot 9H_2O$ solution was added under stirring for 20 min at 100 °C. About 15 mL of HNO_3 (2 M) was added again to the previous solution after cooling the previous solution to room temperature under magnetic stirring. After 15 min, the supernatant was magnetically decanted and washed 2 times with acetone. The product was re-dispersed in water, obtaining a stable water-soluble ferrofluid.

3. Characterization

3.1. Size, dispersion, and morphology

Particle size, size dispersion and morphology of all the fabricated nanostructures were analyzed in a JEOL JEM1010 (JEOL USA, Inc., Peabody, MA) Transmission Electron Microscope (TEM). For TEM analysis, the samples were prepared by diluting the corresponding ferrite ferrofluids in water. A drop of each of the ferrofluids was dispersed over a carbon-coated copper grid and left evaporating at room temperature. The size and size dispersion (σ) of the formed particles were determined by measuring the size of more than 300 individual nanoparticles to construct a histogram; then the histogram was fitted to a lognormal distribution. EDS analysis was carried out in an ultra-high resolution scanning electron microscope MAIA, with a field emission gun at 15 keV.

3.2. Hydrodynamic diameter

The hydrodynamic diameter and size distribution of the nanoparticles in the ferrofluid were determined in their water dispersions at room temperature, using a Nanotrac Wave II, dynamic light scattering (DLS) (Microtrac Inc., Montgomeryville, PA, USA) system, with a 780 nm wavelength laser working at 3 mW power. All the DLS measurements were carried out by diluting the corresponding ferrite ferrofluid in water (refractive index 1.33) until it acquired a yellowish tone. A refractive index of 2.42 was used for all the samples, assuming the changes in the refractive index for the cation-substituted ferrites were negligible.

3.3. Crystallographic analysis

X-ray diffraction (XRD) patterns of the samples were recorded at room temperature using energy filtered Cu Kα radiation (λ = 1.5406 Å) in a PANalytical Empyrean diffractometer, between 10° and 90° of 2θ. The changes in the lattice parameters due to the continuous substitution of the Mn^{2+} ions were determined by means of Rietveld refinement using X'pert Highscore Plus 3.0 software from PANanalytical. The average size of the crystallite was calculated using the Scherrer equation: [24,25]

$$D = \frac{\alpha\lambda}{\beta cos\theta} \qquad (1)$$

where α is a shape factor with a typical value of 0.9 for quasi-spherical nanoparticles, λ is the used X-ray wavelength (1.5406 Å), β represents the FWHM (full width at half maximum) of the (3 1 1) peak and θ is the half of the Bagg angle correspond to the (3 1 1) diffraction peak.

3.4. Ferromagnetic Curie temperature

The ferromagnetic Curie temperature was determined experimentally for all the samples by applying an external magnetic field (50 Oe) and recording the changes in mass with respect to the temperature during their thermogravimetric analysis (TGA). The TGA measurements were carried out in a nitrogen atmosphere, under a flux of 5 mL/min. TGA measurements were performed twice for each sample, the first heating ramp was from room temperature to 800 °C, and then cooling until □ 100 °C. The second heating ramp began when the temperature reached 100 °C, until 800 °C. The Curie temperature was estimated in the second run with an average of the highest point between the heating and the cooling stage.

3.5. Magnetic measurements

Magnetic hysteresis and zero-field cooled (ZFC) curves were recorded in a Dyna-cool 9 physical property measurement system (PPMS, Dyna-cool 9, Quantum Design, USA) by placing the dry powder samples in tubular plastic sample holders. The hysteresis curves were recorded up to a 5 T magnetic field at near room temperature (300 K), 100 K and 10 K. ZFC curves were obtained by cooling the samples up to 10 K, without applying an external magnetic field; then a magnetic field of 200 *Oe* was applied and heating started at a rate of approximately 0.02 K/s until a temperature of 350 K was reached, with the only exception being the sample containing Co^{2+}, where the measurement was performed until 380 K, to monitor its high anisotropy.

4. Results and discussion

4.1. Crystallographic analysis

A crucial characterization to determine the formation of the desired crystalline phase of the samples is X-ray diffraction. Fig. 1 shows the XRD patterns for all the samples. As can be seen, all the patterns are very similar among them, corresponding to a face-centered cubic (FCC) spinel structure, with Fd3m space group [26]. No traces of the corresponding metal oxides (ZnO, FeO, NiO, CoO) from the M^{2+} ions added to substitute the Mn^{2+} ions in the crystal lattice were found; indicating that all the M^{2+} cations were distributed among the A or B sites of the spinel structure. The relative intensities and the signal to noise ratio were the only parameters that visibly changed, indicating different levels of crystallinity or different sizes of the formed crystallites, as have been presented below (Fig. 1).

Taking the most intense peak [(3 1 1) plane] and using the Scherrer equation, the average crystallite size in each of the samples was estimated. The crystallite sizes were 21, 10.8, 11, 11.2 and 14 nm for the samples MnFe$_2$O$_4$, ZnMn, ZnMnFe, ZnMnFeNi, and ZnMnFeNiCo, respectively. These sizes will be compared with TEM results later.

As the Mn^{2+} ions have been substituted by divalent cations with different ionic radii, we can expect changes in the lattice parameters of the host lattice. Rietveld refinement [27,28] of the experimental XRD patterns was performed to determine the changes in the lattice parameter of the host ($MnFe_2O_4$) lattice. Table 1 summarizes the results obtained from the Rietveld refinement.
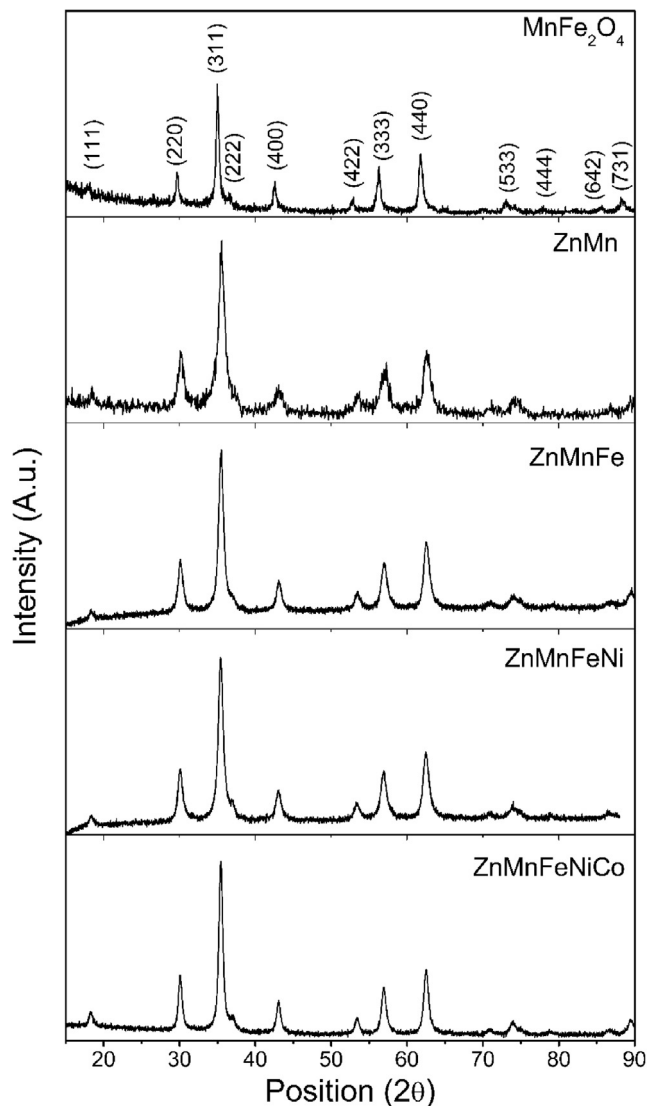

Fig. 1. Powder X-ray diffraction patterns for the manganese ferrite and the substitution of Mn^{2+} with Zn, Fe, Ni, Co, JCPDS # 01-074-2403.

Table 1
Refined lattice parameters with standard deviation and Goodness of Fitness (GOF).

Sample	Composition	Lattice parameter (Å)	GOF
MnFe$_2$O$_4$	MnFe$_2$O$_4$	8.4866(1)	1.4
ZnMn	Zn$_{0.5}$Mn$_{0.5}$Fe$_2$O$_4$	8.4051(5)	2.07
ZnMnFe	Zn$_{0.4}$Mn$_{0.4}$Fe$_{2.2}$O$_4$	8.4032(9)	2.08
ZnMnFeNi	Zn$_{0.3}$Mn$_{0.3}$Ni$_{0.2}$Fe$_{2.2}$O$_4$	8.4141(1)	2.09
ZnMnFeNiCo	Zn$_{0.2}$Mn$_{0.2}$Ni$_{0.2}$Co$_{0.2}$Fe$_{2.2}$O$_4$	8.4090(2)	1.91

4.2. Size, dispersion, and morphology

Analysis of the TEM images (Fig. 2) suggests no significant variation in size and morphology of the nanoparticles after M^{2+} substitution. All the samples revealed similar average particle sizes, except for the pure manganese ferrite, $MnFe_2O_4$, which had the largest particle size (average diameter: 23.7 nm). The sample with the smallest average particle size was the manganese zinc ferrite, ZnMn (average diameter: 8.3 nm). The decrease in particle size by the addition of Zn^{2+} ions was previously observed and reported [29]. The average particle size of all the other samples remained in between 10 and 17 nm (Fig. 3). The results obtained from the TEM analysis strongly correlates with the
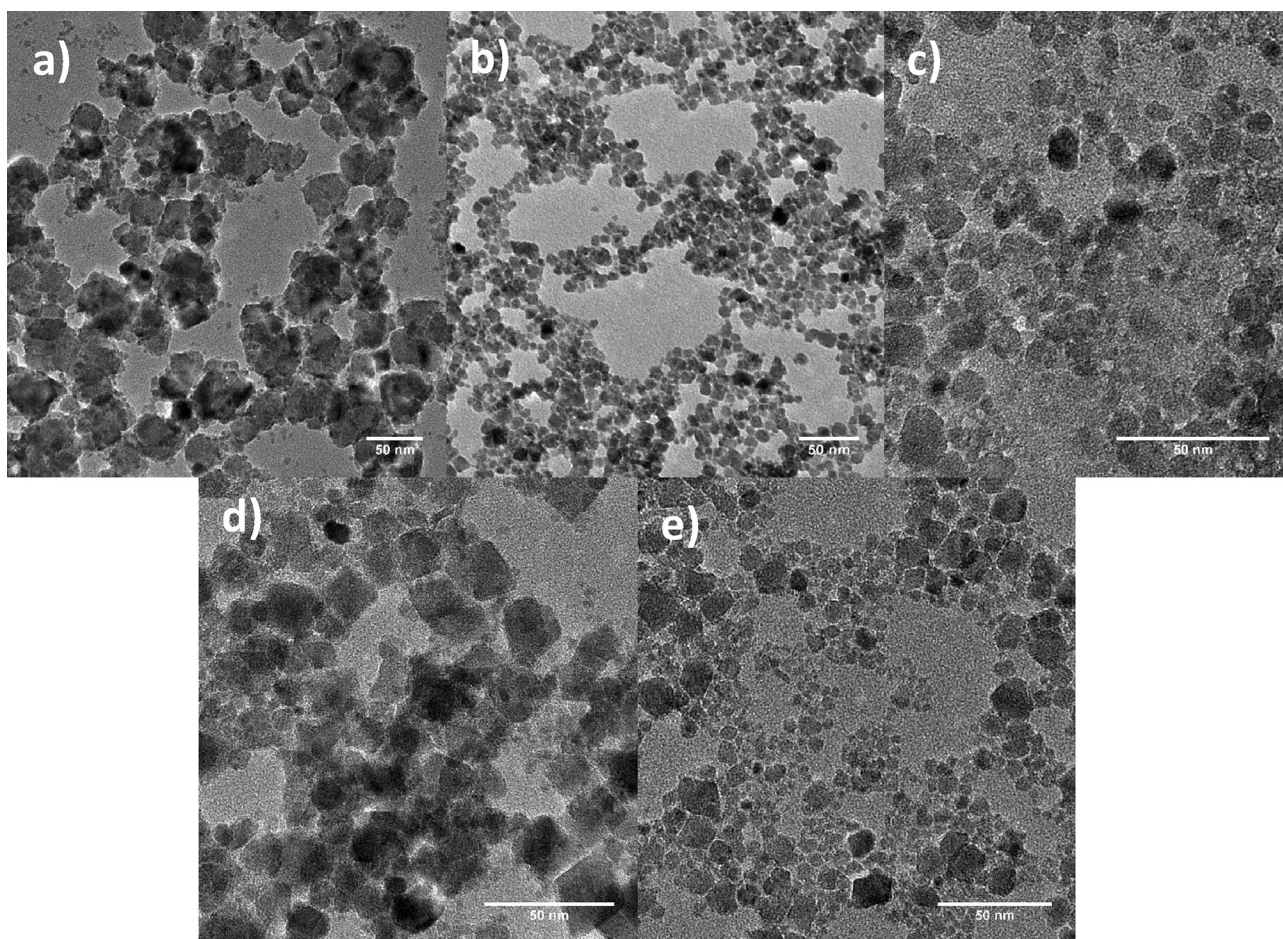
Fig. 2. Typical TEM images of the sample a) MnFe$_2$O$_4$, b) ZnMn, c) ZnMnFe, d) ZnMnFeNi and e) ZnMnFeNiCo. The white bar represents a scale of 50 nm in all the cases.

crystallite size determined previously using the Scherrer equation. In all samples, the smaller particles presented a quasi-spherical shape; however, bigger nanoparticles presented different morphologies. For example, the ZnMnFeNi nanoparticle showed sharper edges than the rest of the samples, and it presented the highest dispersion value at $\sigma = 0.75$.

Although the shape and the average size of the ferrite nanoparticles showed no drastic change after M^{2+} cation substitution, size dispersion changed for samples ZnMnFe ($\sigma = 0.41$) and ZnMnFeNi ($\sigma = 0.75$), as indicated by the size distribution histograms presented in Fig. 3. The other samples presented almost the same size dispersion value ($\sigma \approx 0.25$), as obtained from the fitting of the histograms to the lognormal distribution, even though the sample ZnMn (Fig. 2b) had lower agglomeration and, therefore, their grain boundaries were more defined.

4.3. Elemental analysis

EDS results of the atomic percentage of the metal ions are shown in Table 2. Fe values are taken as total iron in the samples since it is impossible to discriminate from Fe^{2+} and Fe^{3+} by using this technique. From Table 2 it can be seen that in all the samples the Fe ion was much higher than expected, even in the case where no Fe^{2+} had been added to the sample. Furthermore, the Zn and the Ni ions were in less proportion than expected from the nominal value, suggesting that those ions are more difficult to incorporate to the structure than Mn or Fe. The variations from the nominal and the experimental values are due to the different precipitation rates of the different M^{2+} ions, it can be seen that the manganese has the fastest precipitation rate, while Zn and Ni

have the lowest rate.

4.4. Hydrodynamic diameter

Although the hydrodynamic diameter of the samples (Fig. 4) doesn't exactly correspond to the TEM values, the tendency is similar for both characterizations [30]. MnFe$_2$O$_4$ had the largest hydrodynamic diameter followed by ZnMnFeNiCo, in agreement with the previously discussed TEM results. The only variation is that while ZnMn and ZnMnFe had the lowest and second lowest diameters, respectively, as shown by TEM images, the hydrodynamic diameter for ZnMnFe revealed the lowest value, followed by ZnMn, with a difference of just a few nanometers. This was the only variation in the size trend as determined by TEM and DLS. Nevertheless, all the samples presented hydrodynamic diameters lower than 100 nm, which means that they were stable in water and do not aggregate in aqueous solution. This is a very important requirement for the design of nanomaterials for medical application, especially in the case of magnetic nanoparticles, as their magnetic dipoles attract each other, inducing aggregation and precipitation. This result proved the convenience of the acid treatment to avoid agglomeration of magnetic nanoparticles in water [31–33]. Table 3 summarizes the average sizes obtained from TEM, DLS along with the average crystallite size values estimated from the XRD patterns of the samples.

4.5. Ferromagnetic Curie temperature (T_C)

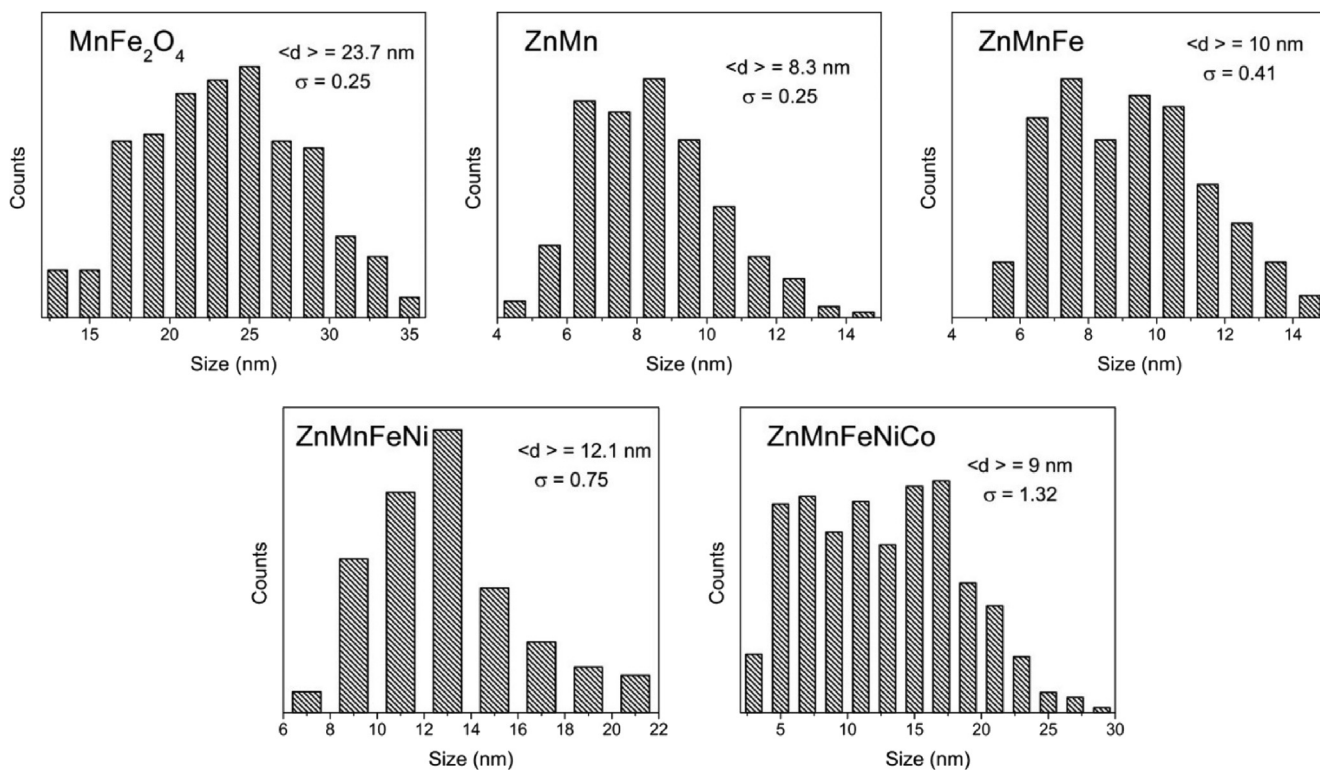In order to measure the T_C, a permanent magnet was placed on top

Fig. 3. Size distribution histograms of the samples fitted to a lognormal distribution function. The average diameter (⟨d⟩) and the dispersion (σ) are indicated for each sample.

Table 2
Atomic percentage nominal (Nom) and experimental (Exp) values of the cations obtained from EDS.

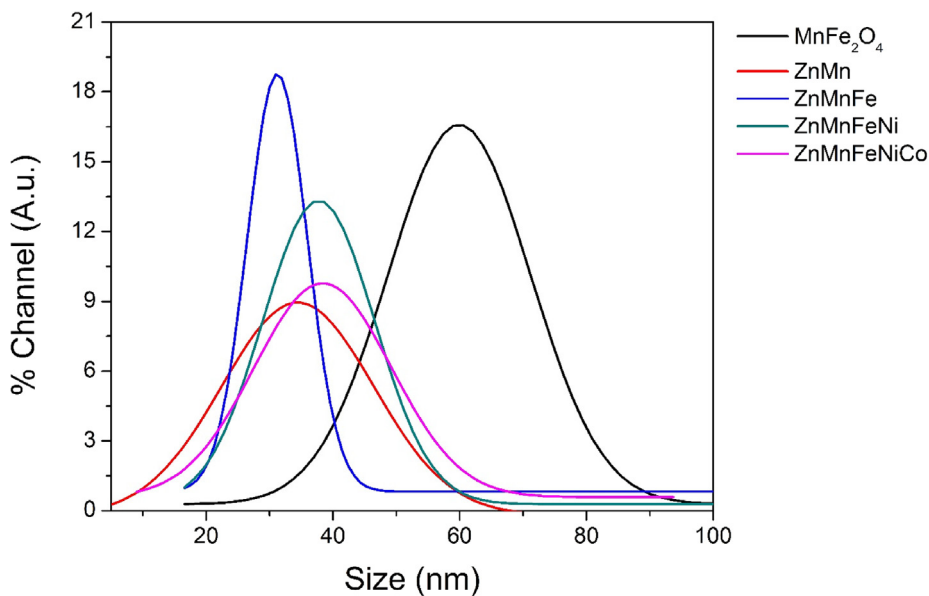|	MnFe$_2$O$_4$		ZnMn		ZnMnFe		ZnMnFeNi		ZnMnFeNiCo	
	Nom	Exp	Nom	Exp	Nom	Exp	Nom	Exp	Nom	Exp
Mn	34%	35%	17%	15%	13%	8%	10%	9%	7%	6%
Zn	–	–	17%	12%	13%	5%	10%	6%	7%	5%
Ni	–	–	–	–	–	–	7%	4%	7%	5%
Co	–	–	–	–	–	–	–	–	7%	6%
Fe^{2+}/Fe^{3+}	66%	65%	66%	73%	74%	87%	73%	81%	72%	78%

Fig. 4. DLS spectra of the colloidal nanoparticles showing their good stability in water.

Table 3

Average size of the nanoparticles estimated from their TEM, DLS analysis and average crystallite size calculated by XRD.

Sample	Composition	TEM (nm)	XRD (nm)	DLS (nm)
MnFe$_2$O$_4$	MnFe$_2$O$_4$	23.7	21	59.9
ZnMn	Zn$_{0.5}$Mn$_{0.5}$Fe$_2$O$_4$	8.3	10.8	34.41
ZnMnFe	Zn$_{0.4}$Mn$_{0.4}$Fe$_{2.2}$O$_4$	10	11	31.2
ZnMnFeNi	Zn$_{0.3}$Mn$_{0.3}$Ni$_{0.2}$Fe$_{2.2}$O$_4$	12.1	11.2	37.72
ZnMnFeNiCo	Zn$_{0.2}$Mn$_{0.2}$Ni$_{0.2}$Co$_{0.2}$Fe$_{2.2}$O$_4$	9	14	38.37

of the TGA to reduce the weight of the sample from 3 to 5%; when the sample reached the T_C, a significative variation in the weight will be observed as the magnetic contribution is no longer affecting the sample. This increase in the weight of the sample is indicative of a transition from a ferrimagnetic phase to a diamagnetic phase.

As different cations substituted the Mn^{2+} ions in the crystalline spinel structure, a change in T_C is expected due to the distortion in the lattice produced by elongation in one axis of the octahedral in order to reduce repulsions known as the Jahn-Teller effect. Fig. 5 shows the TGA curves for all the samples; the measurements were performed twice to avoid the effects of adsorbed components at the surface. The T_C of all the samples can be clearly identified mostly in the second run, where
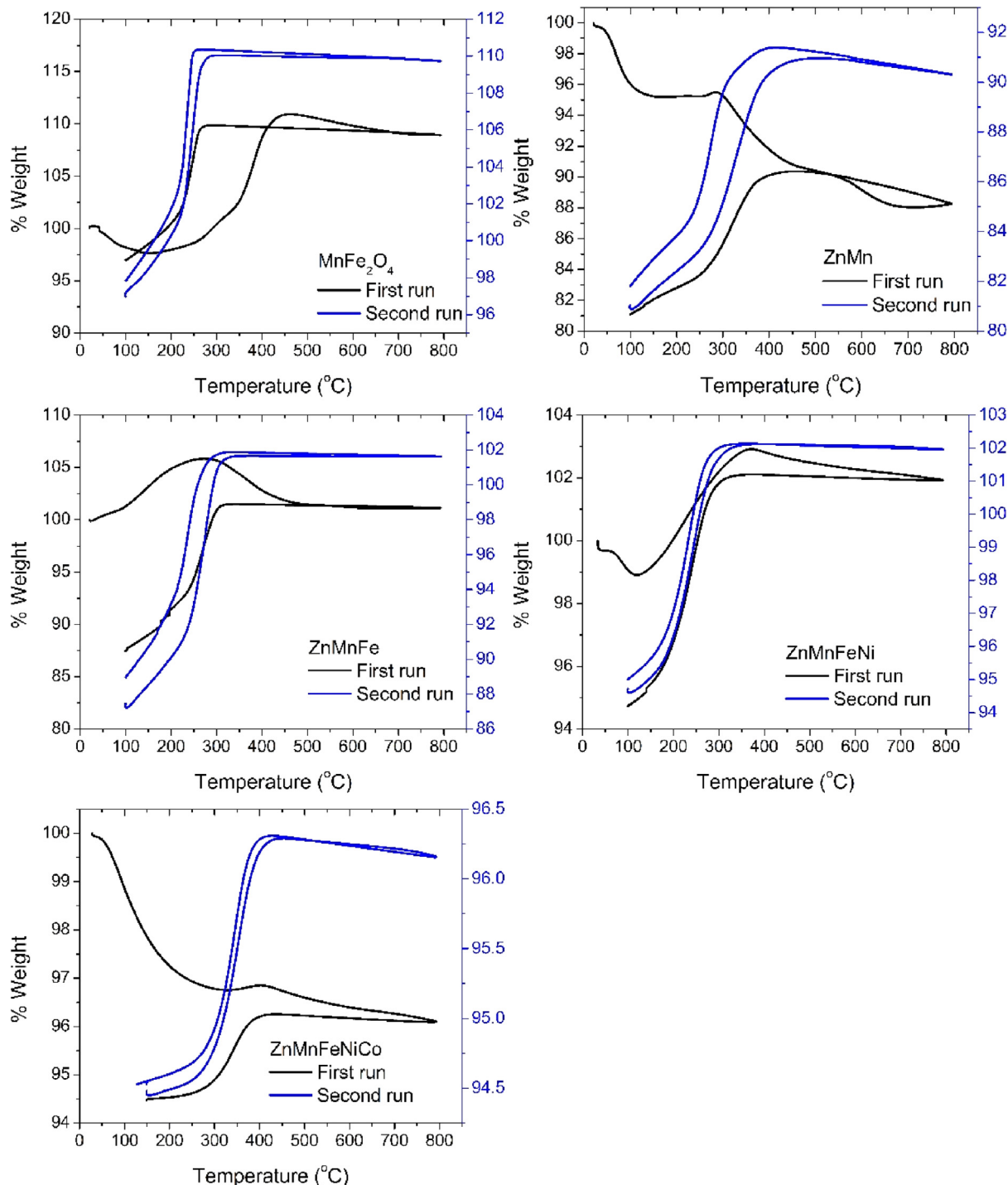

Fig. 5. TGA curves of all the samples showing a clear jump which indicates the Curie temperature.
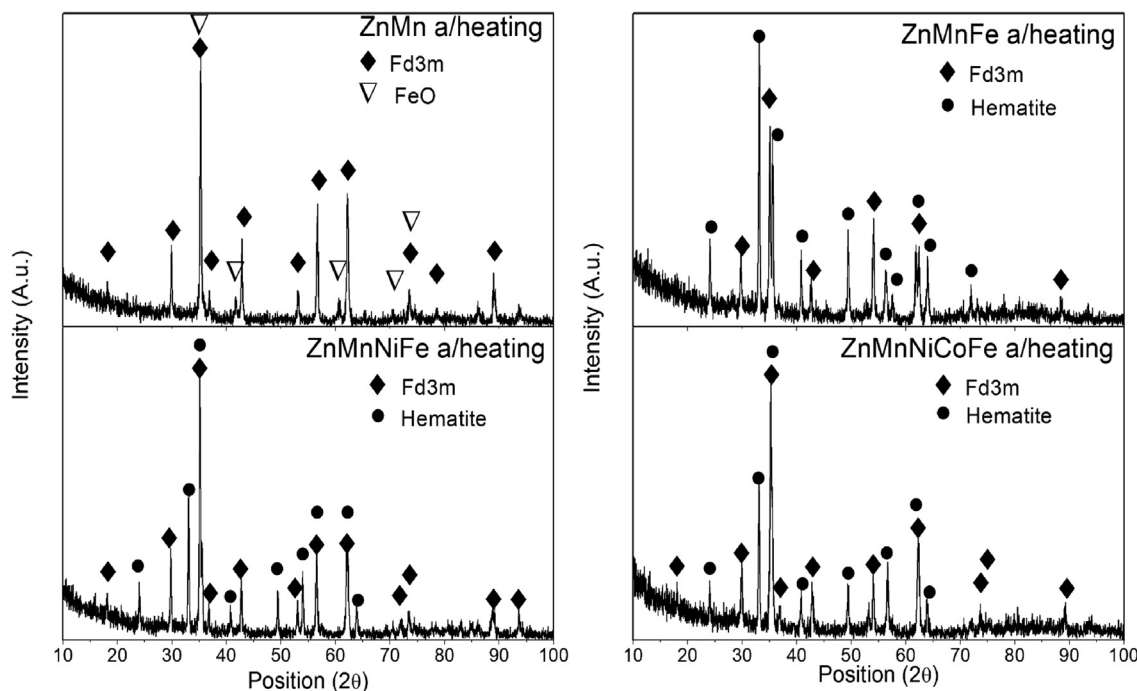
Fig. 6. XRD patterns of the samples after the heating process of the TGA JCPDS for FeO #01-074-1886, Hematite # 00-002-0915.
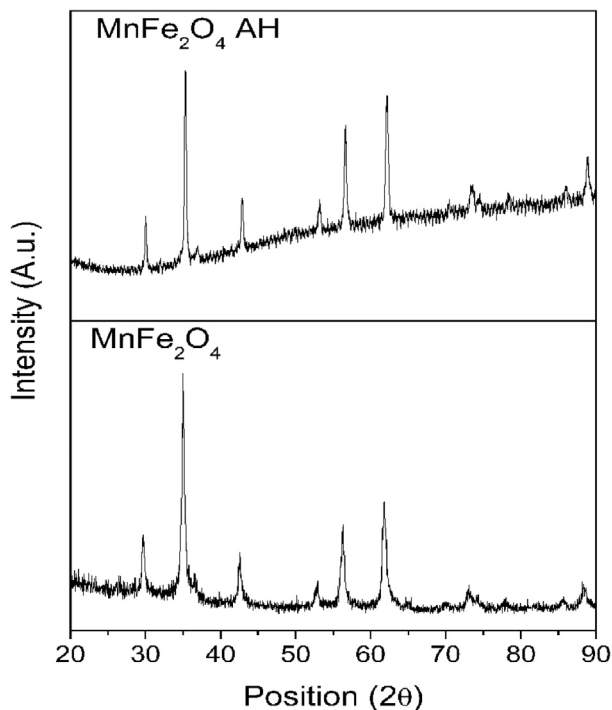

Fig. 7. XRD patterns of sample $MnFe_2O_4$ recorded after TGA analysis, indicating that there was no change after the heating (AH) process.

Table 4
Rietveld analysis of the samples after the heating process.

Sample	Composition	% Ferrite	% Hematite
$MnFe_2O_4$	$MnFe_2O_4$	100%	0%
ZnMnFe	$Zn_{0.4}Mn_{0.4}Fe_{2.2}O_4$	72.10%	27.90%
ZnMnFeNi	$Zn_{0.3}Mn_{0.3}Ni_{0.2}Fe_{2.2}O_4$	84.20%	15.80%
ZnMnFeNiCo	$Zn_{0.2}Mn_{0.2}Ni_{0.2}Co_{0.2}Fe_{2.2}O_4$	83.90%	16.10%

the weight increment is more pronounced. The weight variation is reversible when cooling the samples. For most of the cases, the jumps (the temperature of phase transition) during heating and cooling match each other; except for sample ZnMnFe, where there is a slight variation between the values revealed during heating and cooling [34].

The sample $MnFe_2O_4$ presented a T_c of 265 °C, this value increased for the ZnMn to 415 °C, and decreased to 314 °C for ZnMnFe. For the next cation addition, the T_c remained almost the same at 319 °C (ZnMnFeNi) and for the last cation addition, the T_c increased to 432 °C. The T_c also showed the previously observed trend where samples ZnMnFe and ZnMnFeNi presented almost the same properties, this may be due to the fact that experimental values of the atomic percentage of the M^{2+} ions are relatively in the same proportion in both samples, as seen from Table 2. It should be noticed that adding cobalt ions resulted in an increment of the T_c value.

Because the color of the powders used for the thermogravimetric analysis visibly changed after the measurements, new XRD patterns were collected after their TGA analysis. Fig. 6 shows the XRD patterns obtained for the samples after their use in TGA analysis.

There is a clear change in the XRD patterns of the samples before and after the heating process in the TGA. A new crystalline phase appears after the thermal treatment. For the sample ZnMn, the newly appeared diffraction peaks correspond to a rock salt crystal structure, possibly wustite (FeO). For the other samples, the newly formed peaks clearly correspond to a hematite phase (α-Fe_2O_3 with a space group R-3C). Sample $MnFe_2O_4$ does not present a big change in the XRD pattern under the conditions the time and temperature conditions applied here, as Fig. 7 show.

These results can explain why the T_c values of all the samples appear to be similar in the second run. The Mn^{2+} cations substituted from the spinel lattice created a metastable pure ferrite, as Fig. 1 shows. On heating the sample, it suffers a phase transition to form iron oxide and a non-stoichiometric ferrite. These phase transitions due to metastable phases are a crucial factor to consider when designing a magnetic material. In the case of these samples, heating is enough to produce a phase structure transition before a magnetic transition (T_c) when the material is highly doped. Nevertheless, an undoped manganese ferrite can stand heating up to 800 °C degrees with no changes in its structure.
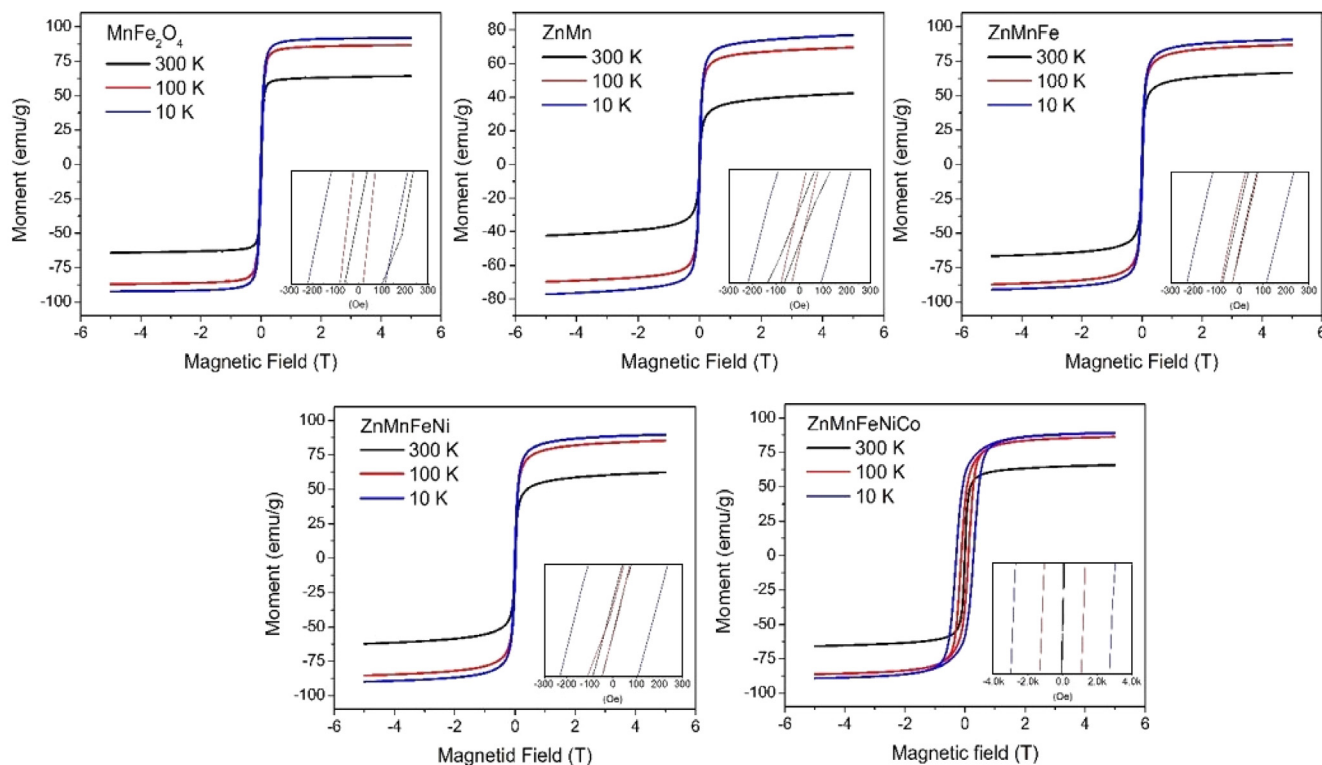
Fig. 8. Hysteresis curves of the different Mn^{2+} substituted samples.

Table 5
Magnetic saturation values of the samples before heating at different temperatures and the loss in magnetization in compare to the 10 K value.

Sample	Composition	10 K (emu/g)	100 K (emu/g)	% loss	300 K (emu/g)	% loss
MnFe2O4	$MnFe_2O_4$	92	86	6.5	64	30.4
ZnMn	$Zn_{0.5}Mn_{0.5}Fe_2O_4$	77	69	10.3	43	44.1
ZnMnFe	$Zn_{0.4}Mn_{0.4}Fe_{2.2}O_4$	90	86	4.4	66	26.6
ZnMnFeNi	$Zn_{0.3}Mn_{0.3}Ni_{0.2}Fe_{2.2}O_4$	90	85	5.5	62	31.1
ZnMnFeNiCo	$Zn_{0.2}Mn_{0.2}Ni_{0.2}Co_{0.2}Fe_{2.2}O_4$	89	86	3.3	66	25.8

Unfortunately, it is very difficult to identify the non-stoichiometric ferrite produced by the phase transition of the highly substituted ferrites, as all the ferrites have very similar XRD patterns. Moreover, Fe, Ni, Co, and Zn have almost the same properties and energies, e.g., the $K\alpha$ values are 5.89, 6.39, 6.9 and 7.4 for manganese, iron, nickel, and cobalt, respectively. These common characteristics between the M^{2+} ions, in addition to the small size (< 20 nm) of the nanoparticles make really difficult to have a reliable elemental mapping of the samples.

Rietveld analysis of the new XRD patterns was performed to determine the percentage of each of the phases formed. Table 4 shows the results of this refinement.

4.6. Magnetic measurements

All the metal cations used to substitute Mn^{2+} are well-known to produce magnetic ferrites [35,36], except the Zn^{2+}, which is a diamagnetic ion. However, the substitution of Mn^{2+} from $MnFe_2O_4$ lattice by Zn^{2+} has been performed regularly as it increases the biocompatibility of the whole material. Likewise, it has been reported that the incorporation of Zn^{2+} causes a small reduction of magnetic saturation (M_s) of the ferrite [37].

The sample with the highest magnetization at 10 K and 100 K was $MnFe_2O_4$ with values of 92 and 86 emu/g, respectively, at the mentioned temperatures. On the other hand, the sample ZnMnFe along with the sample ZnMnFeNiCo had the highest M_s value at 300 K (M_s = 66 emu/g). In addition, as expected, the sample ZnMn had the lowest M_s value at all the measured temperatures due to the presence of diamagnetic zinc ions. The hysteresis curves can be seen in Fig. 8.

Although $MnFe_2O_4$ had the highest M_s value at 10 and 100 K, its M_s considerably decrease at 300 K with respect to the other samples. The M_s values decrease with respect to the temperature because the thermal energy ($E_T = k_BT$) [38,39] produces vibration of the magnetic dipoles of the nanoparticles, slightly dis-aligning the magnetic moment with respect to the external magnetic field. Table 5 shows the M_s values of the samples along with the percentage of the saturation loss due to heating from 10 K to 100 K.

The sample ZnMnNiCoFe had the lowest M_s loss among all the samples, while the sample ZnMn had the highest M_s loss. This behavior can be related to the coercivity of the samples. Coercivity is defined as the amount of energy that is necessary to demagnetize the material, thus high coercivity values mean that the spin is more confined or blocked. Usually, Co shows a distinctive high coercivity value. As can be seen, on incorporating Co^{2+} ions, the coercivity increased drastically from ☐ 200 Oe to 2000 Oe at 10 K. None of the other metal ions incorporated in the $MnFe_2O_4$ lattice revealed such a significant increment in coercivity. Also, as Zn^{2+} ions do not actively contribute to the overall magnetism, the sample ZnMn had the lowest coercivity values.

Furthermore, the Bohr magnetons (μ_B) reported for the individual ferrites are 5 μ_B for $MnFe_2O_4$, 4 μ_B for Fe_3O_4, 3 μ_B for $CoFe_2O_4$, and 2 μ_B for $NiFe_2O_4$ [40] this variations are in agreement with behavior of the magnetic saturation of the samples, being the $MnFe_2O_4$ the sample with the highest M_s and when Ni^{2+} are introduced the saturation decreased.
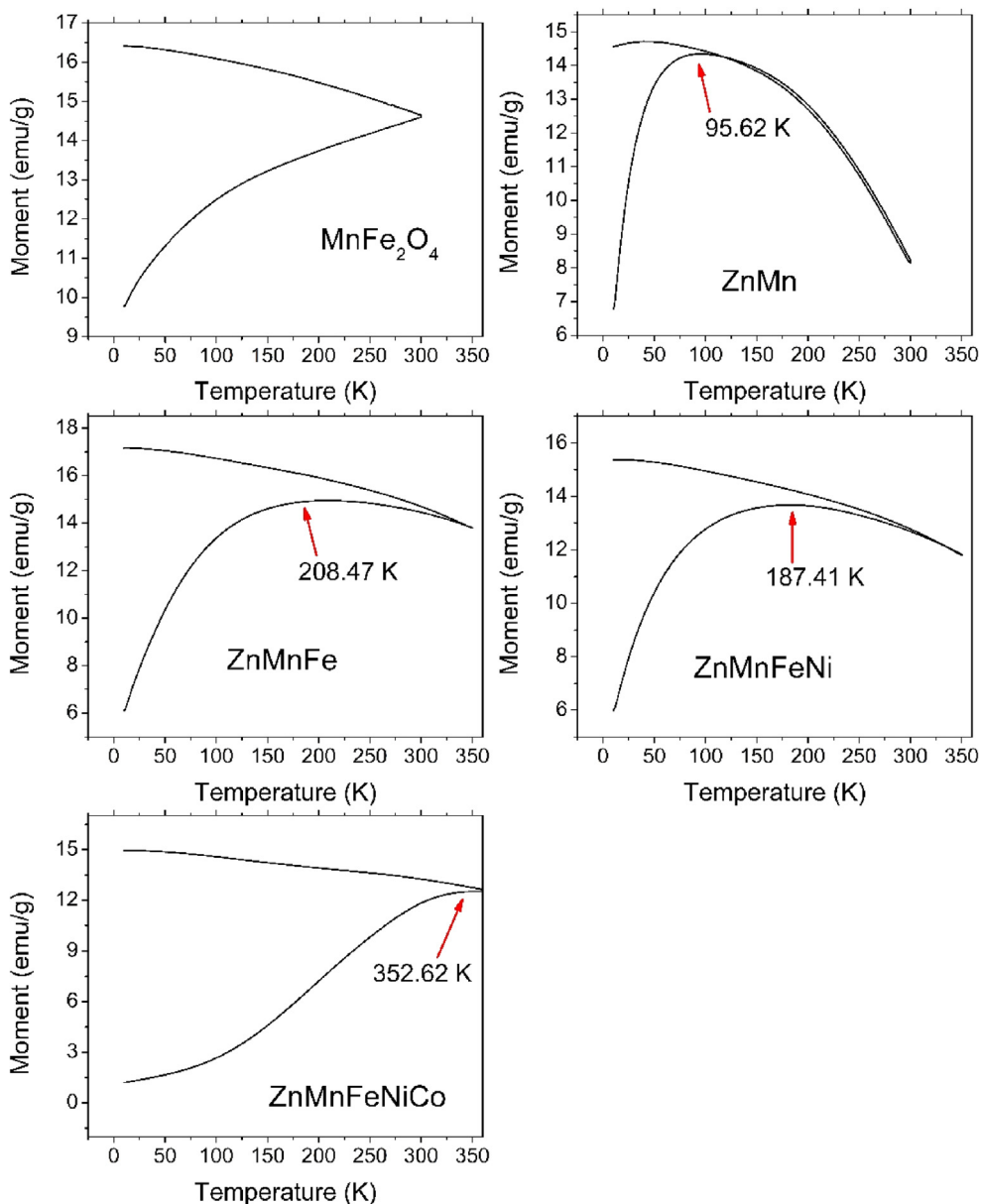
Fig. 9. ZFC graphs of all the samples, the blocking temperature is shown with a red arrow. (For interpretation of the references to color in this figure legend, the reader is referred to the web version of this article.)

Table 6
Summary of the size and magnetic properties of the samples.

Sample	TEM (nm)	M_s 10 K (emu/g)	M_s 300 K (emu/g)	T_B (K)	K_{eff} (kJm^{-3})
MnFe$_2$O$_4$	23.7	92	64	> 300	26
ZnMn	8.3	77	43	95	4
ZnMnFe	10	90	66	208	17
ZnMnFeNi	12.1	90	62	187	11
ZnMnFeNiCo	9	89	66	352	84

ZnFe$_2$O$_4$ is not considered because it is mostly antiferromagnetic in nature.

The effective anisotropy of the samples (K_{eff}) was calculated by using the following formula derived from elsewhere [41]:

$$K_{eff} = \frac{\mu_0 M_s H_c}{2} + \frac{50 k_B T}{V}$$

where μ_0 is the permeability of free space (1.256 NA^{-2}), M_s is the magnetic saturation and H_c is the coercivity, both in units A/m, k_B is the Boltzmann constant (1.38 × 10^{-23} JK^{-1}), T is the temperature in K and V is the average volume of the nanoparticles considering that all the samples are spherical. The obtained K_{eff} values were 26, 4, 17, 11 and 84 kJm^{-3} which also correlates with the coercivities on the inset in Fig. 8.

From Fig. 8, all the samples except ZnMnFeNiCo appear to have a superparamagnetic behavior at room temperature, meaning that they do not possess considerable magnetic remanence (M_r) or coercivity (H_c), however, ZFC-FC curves are needed to confirm this superparamagnetic state.

The relationship between the coercivity and E_T can also be seen in the zero-field cooled graphs (Fig. 9). At the blocking temperature (T_B), all the blocked spins become free. Below the T_B the spins of the sample are almost completely blocked and cannot move freely, nor can rotate. However, above the T_B, the contribution of the thermal energy is enough to allow rotation of the spins of the sample [42].

The T_B can be determined as the temperature with the highest value

of magnetization in the ZFC curve. The lowest T_B corresponds exactly to the ZnMn sample, and the highest T_B corresponds to the ZnMnFeNiCo sample, as expected. The exception, in this case, was the MnFe$_2$O$_4$ sample, which as stated before, had a low coercivity, and hence should have a low T_B temperature. However, the ZFC curve of the sample (Fig. 9a) did not reveal a clear T_B in the whole range measured temperature. This behavior can be explained considering the Néel relaxation model [41].

$$\tau = \tau_0 e^{E_B/E_T}$$

where τ_0 is the attempt time, a characteristic time of the sample usually between 10^{-9}–10^{-10} s, and E_B is the energy barrier. This energy barrier depends on the effective anisotropy and the average volume of the nanoparticles ($E_B = V*K_{eff}$). As has been shown in Section 4.2, the average particles size for all the samples are similar, with the exception of MnFe$_2$O$_4$, which had larger particle diameters. Due to this larger particle diameters, the E_B for the MnFe$_2$O$_4$ sample is larger in comparison with the E_B values of all the other smaller samples thus increasing its T_B. Table 6 shows a summary of the size and the magnetic properties of the samples.

5. Summary

The sample ZnMn had the lowest size, and M_s at both temperatures (10 and 300 K), the lowest K_{eff}, which leads to the lowest T_B. The reason behind this sample having the lowest values is due to the high concentration of the diamagnetic Zn ion, as Table 2 shows this sample had the highest Zn concentration of them all. The small size of this sample can be another factor influencing these properties, nevertheless, the rest of the samples have similar sizes, but considerably higher values of M_s.

Although the sample ZnMnNiCo showed an average diameter of only 9 nm, it had the highest M_s at 300 K, even being the sample with the lowest Mn^{2+} concentration according to Table 2, which is the ions that contribute more to the M_s. This behavior can be explained due to the introduction of Co, which is a highly anisotropic ion; the high anisotropy of Co ion increased the overall coercivity and anisotropy, thus increasing the T_B. In addition, the high anisotropy of the Co and the large T_B value, made possible to reduced the loss of the M_s due to heat effects, which is the reason this sample presented the highest room temperature M_s.

According to Ref. [40], MnFe$_2$O$_4$ had the highest μ_B, this is clearly seen at the 10 K M_s value. Even Mn^{2+} ion had low coercivity and anisotropy, the large size of this sample resulted in a high coercivity and a high T_B. According to the EDS measurements, the chemical composition of this sample is extremely close to the nominal values.

The samples ZnMnFe and ZnMnFeNi presented similar properties between them, even at 10 K they had the same M_s. The similar properties between them can be the result of both having a similar composition of Mn and Zn and the main difference is in the quantity of Fe (Table 2). Moreover, ZnMnFe sample should have a higher M_s than ZnMnFeNi as Fe had larger μ_B than Ni, still, ZnMnFeNi had a larger size than ZnMnFe, and because of this, both samples have the same M_s at 10 K. The T_B and the M_s at 300 K slightly differs, however, this change can be attributed mainly to the anisotropy of the sample, meaning that the Fe is a more anisotropic ion than Ni.

6. Conclusion

In this work, the effects of the systematic substitution of M^{2+} ions (M = Zn, Fe, Ni, Co) in manganese ferrite (MnFe$_2$O$_4$) nanoparticles was presented. The manganese ion was easily substituted, as no other crystalline phase was found at the X-rays diffraction patterns, suggesting that the Mn^{2+} ions were effectively replaced into the ferrite structure. However, this substitution yields a meta-stable crystalline phase, which can decompose into two different metal oxide crystalline phases after thermal heating. After the ZnMn ferrite was heated, a FeO

phase formed as indicated by XRD. Pure MnFe$_2$O$_4$ does not appear to present any relevant structural change after the heating process up to 800 °C. It was also demonstrated that the changes in the magnetic properties were commensurable with the nature of the transition metal ion used for substitution of the Mn^{2+} ion. The physical properties for samples ZnMnFe and ZnMnFeNi were alike, suggesting that substitution by Fe^{2+} or Ni^{2+} in small quantities produces no significative structural or magnetic changes. Finally, for the structure of the ferrite, the magnetic properties such as the coercivity and the blocking temperature (T_B) can be easily tailored by selecting appropriately the M^{2+} ion used for substitution. For a drastic reduction of the coercivity and blocking temperature, Zn^{2+} is an effective way to achieve that, with the downside of decreasing the magnetic saturation (M_s). Substitution with Fe^{2+} and Ni^{2+} also reduces the coercivity and blocking temperature without affecting considerably the magnetic saturation; in contrast, even a tiny addition of Co^{2+} produces the contrary effect by increasing both the coercivity and blocking temperatures.

References

[1] B.J. Evans, Magnetism and archaeology: magnetic oxides in the first american civilization, Phys. B + C 86–88 (1977) 1091–1099.

[2] M.M. Baig, M.A. Yousuf, P.O. Agboola, M.A. Khan, I. Shakir, M.F. Warsi, Optimization of wet chemical routes and phase evolution studies of MnFe$_2$O$_4$ nanoparticles, Ceram. Int. (2019), https://doi.org/10.1016/j.ceramint.2019.03.114.

[3] C. Ravikumar, R. Bandyopadhyaya, Mechanistic study on magnetite nanoparticle formation by thermal decomposition and coprecipitation routes, J. Phys. Chem. C. 115 (2011) 1380–1387, https://doi.org/10.1021/jp105304w.

[4] M. Unni, A.M. Uhl, S. Savliwala, B.H. Savitzky, R. Dhavalikar, N. Garraud, D.P. Arnold, L.F. Kourkoutis, J.S. Andrew, C. Rinaldi, Thermal decomposition synthesis of iron oxide nanoparticles with diminished magnetic dead layer by controlled addition of oxygen, ACS Nano. 11 (2017) 2284–2303, https://doi.org/10.1021/acsnano.7b00609.

[5] D.L. Leslie-Pelecky, R.D. Rieke, Magnetic properties of nanostructured materials, Chem. Mater. 8 (1996) 1770–1783, https://doi.org/10.1021/cm960077f.

[6] M.K. Surendra, S. Kanti De, M.S.R. Rao, Application worthy SPIONs: coated magnetic nanoparticles, IEEE Trans. Magn. 50 (2014) 2–7, https://doi.org/10.1109/TMAG.2014.2305644.

[7] M.A. Radmanesh, S.A. Seyyed Ebrahimi, Synthesis and magnetic properties of hard/soft SrFe$_{12}$O$_{19}$/Ni$_{0.7}$Zn$_{0.3}$Fe$_2$O$_4$ nanocomposite magnets, J. Magn. Magn. Mater. 324 (2012) 3094–3098, https://doi.org/10.1016/j.jmmm.2012.05.008.

[8] G.C. Papaefthymiou, Nanoparticle magnetism, Nano Today. 4 (2009) 438–447, https://doi.org/10.1016/j.nantod.2009.08.006.

[9] P. Poddar, J.L. Wilson, H. Srikanth, S.A. Morrison, E.E. Carpenter, Magnetic properties of conducting polymer doped with manganese–zinc ferrite nanoparticles, Nanotechnology 15 (2004) S570–S574, https://doi.org/10.1088/0957-4484/15/10/013.

[10] F. Arteaga-Cardona, E. Gutiérrez-García, S. Hidalgo-Tobón, C. López-Vasquez, Y.A. Brito-Barrera, J. Flores-Tochihuitl, A. Angulo-Molina, J.R. Reyes-Leyva, R. González-Rodríguez, J.L. Coffer, U. Pal, M.P.-P. Diaz-Conti, D. Platas-Neri, P. Dies-Suarez, R.S. Fonseca, O. Arias-Carrión, M.A. Méndez-Rojas, Cell viability and MRI performance of highly efficient polyol-coated magnetic nanoparticles, J. Nanoparticle Res. 18 (2016), https://doi.org/10.1007/s11051-016-3646-0.

[11] J. Kanamori, Superexchange interaction of electron and symmetry, J. Phys. Chem. Solids. 10 (1959) 87–98.

[12] D. Ortega, Q.A. Pankhurst, Magnetic hyperthermia, (2013) 60–88. doi:10.1039/9781849734844-00060.

[13] A.D. Arelaro, E. Lima, L.M. Rossi, P.K. Kiyohara, H.R. Rechenberg, Ion dependence of magnetic anisotropy in MFe2O4 (M = Fe Co, Mn) nanoparticles synthesized by high-temperature reaction, J. Magn. Magn. Mater. 320 (2008) 335–338, https://doi.org/10.1016/j.jmmm.2008.02.066.

[14] Y. Il Kim, D. Kim, C.S. Lee, Synthesis and characterization of CoFe$_2$O$_4$ magnetic nanoparticles prepared by temperature-controlled coprecipitation method, Phys. B Condens. Matter. 337 (2003) 42–51, https://doi.org/10.1016/S0921-4526(03)00322-3.

[15] V.M. Khot, A.B. Salunkhe, N.D. Thorat, R.S. Ningthoujam, S.H. Pawar, Induction heating studies of dextran coated MgFe$_2$O$_4$ nanoparticles for magnetic hyperthermia, Dalt. Trans. 42 (2013) 1249–1258, https://doi.org/10.1039/C2DT31114C.

[16] E.L. Verde, G.T. Landi, J.A. Gomes, M.H. Sousa, A.F. Bakuzis, Magnetic hyperthermia investigation of cobalt ferrite nanoparticles: comparison between experiment, linear response theory, and dynamic hysteresis simulations, J. Appl. Phys. 111 (2012), https://doi.org/10.1063/1.4729271.

[17] J. Qu, G. Liu, Y. Wang, R. Hong, Preparation of Fe$_3$O$_4$-chitosan nanoparticles used for hyperthermia, Adv. Powder Technol. 21 (2010) 461–467, https://doi.org/10.1016/j.apt.2010.01.008.

[18] M.H. Abdellatif, G.M. El-Komyb, A.A. Azab, Magnetic characterization of rare earth doped spinel ferrite M. J. Magn. Magn. Mater. 442 (2017), https://doi.org/10.1016/j.jmmm.2017.07.020.

[19] L. Zhao, H. Yang, X. Zhao, L. Yu, Y. Cui, S. Feng, Magnetic properties of $CoFe_2O_4$ ferrite doped with rare earth ion, Mater. Lett. 60 (2006) 1–6, https://doi.org/10.1016/j.matlet.2005.07.017.

[20] M.A. Yousuf, M.M. Baig, N.F. Al-khalli, M.A. Khan, M.F.A. Aboud, I. Shakir, M.F. Warsi, The impact of yttrium cations (Y^{3+}) on structural, spectral and dielectric properties of spinel manganese ferrite nanoparticles, Ceram. Int. (2019), https://doi.org/10.1016/j.ceramint.2019.02.174.

[21] M. Veverka, K. Závěta, O. Kaman, P. Veverka, K. Knížek, E. Pollert, M. Burian, P. Kašpar, Magnetic heating by silica-coated Co–Zn ferrite particles, J. Phys. D. Appl. Phys. 47 (2014) 065503, , https://doi.org/10.1088/0022-3727/47/6/065503.

[22] M. Jeun, S. Park, G.H. Jang, K.H. Lee, Tailoring $Mg_xMn_{1-x}Fe_2O_4$ superparamagnetic nanoferrites for magnetic fluid hyperthermia applications, ACS Appl. Mater. Interfaces. 6 (2014) 16487–16492, https://doi.org/10.1021/am5057163.

[23] F. Arteaga-Cardona, S. Hidalgo-Tobón, U. Pal, M.Á. Méndez-Rojas, Ferrites as magnetic fluids for hyperthermia and MRI contrast agents, AIP Conf. Proc. (2016), https://doi.org/10.1063/1.4954118.

[24] J.I. Langford, A.J.C. Wilson, Scherrer after sixty years: a survey and some new results in the determination of crystallite size, J. Appl. Crystallogr. 11 (1978) 102–113, https://doi.org/10.1107/S0021889878012844.

[25] A. Monshi, M.R. Foroughi, M.R. Monshi, Modified scherrer equation to estimate more accurately nano-crystallite size using XRD, World J. Nano Sci. Eng. 02 (2012) 154–160, https://doi.org/10.4236/wjnse.2012.23020.

[26] H.P. Rooksby, B.T.M. Willis, Crystal structure and magnetic properties of cobalt ferrite at low temperatures, Nat. Publ. Gr. 172 (1953).

[27] H.-M. Song, J.I. Zink, N.M. Khashab, Seeded growth of ferrite nanoparticles from Mn oxides: observation of anomalies in magnetic transitions, Phys. Chem. Chem. Phys. 17 (2015) 18825–18833, https://doi.org/10.1039/C5CP01301A.

[28] R. Safi, A. Ghasemi, R. Shoja-razavi, E. Ghasemi, T. Sodaee, Rietveld structure refinement, cations distribution and magnetic features of $CoFe_2O_4$ nanoparticles synthesized by co-precipitation, hydrothermal, and combustion methods, Ceram. Int. 42 (2016), https://doi.org/10.1016/j.ceramint.2016.01.032.

[29] E. Auzans, D. Zins, E. Blums, R. Massart, Synthesis and properties of Mn-Zn ferrite ferrofluids, J. Mater. Sci. 34 (1999) 1253–1260, https://doi.org/10.1023/A:1004525410324.

[30] J. Lim, S. Yeap, H. Che, S. Low, Characterization of magnetic nanoparticle by dynamic light scattering, Nanoscale Res. Lett. 8 (2013) 381, https://doi.org/10.1186/1556-276X-8-381.

[31] F. Arteaga-Cardona, K. Rojas-Rojas, R. Costo, M.A. Mendez-Rojas, A. Hernando, P. De La Presa, Improving the magnetic heating by disaggregating nanoparticles, J. Alloys Compd. 663 (2016), https://doi.org/10.1016/j.jallcom.2015.10.285.

[32] B. Bittova, J.P. Vejpravova, M.P. del Morales, A.G. Roca, D. Niznansky,

A. Mantlikova, Influence of aggregate coating on relaxations in the systems of iron oxide nanoparticles, Nano. 07 (2012) 1250004, https://doi.org/10.1142/S179329201250004X.

[33] S. Mornet, S. Vasseur, F. Grasset, P. Veverka, G. Goglio, A. Demourgues, J. Portier, E. Pollert, E. Duguet, Magnetic nanoparticle design for medical applications, Prog. Solid State Chem. 34 (2006) 237–247, https://doi.org/10.1016/j.progsolidstchem.2005.11.010.

[34] F. Arteaga-Cardona, N.G. Martha-Aguilar, J.O. Estevez, U. Pal, M.Á. Méndez-Rojas, U. Salazar-Kuri, Variations in magnetic properties caused by size dispersion and particle aggregation on $CoFe_2O_4$, SN Appl. Sci. 1 (2019) 412, https://doi.org/10.1007/s42452-019-0447-y.

[35] F.A. Cardona, E.S. Urquiza, P. de la Presa, S.H. Tobón, U. Pal, P.H. Fraijo, M.J. Yacaman, J.D. Lozada Ramírez, R. Ivkov, A. Angulo-Molina, M.Á. Méndez-Rojas, Enhanced magnetic properties and MRI performance of bi-magnetic core--shell nanoparticles, RSC Adv. 6 (2016) 77558–77568, https://doi.org/10.1039/C6RA14265F.

[36] J. Mohapatra, A. Mitra, D. Bahadur, M. Aslam, Surface controlled synthesis of $MFe2O4$ (M = Mn, Fe Co, Ni and Zn) nanoparticles and their magnetic characteristics, CrystEngComm. 15 (2013) 524–532, https://doi.org/10.1039/C2CE25957E.

[37] B. Behdadfar, A. Kermanpur, H. Sadeghi-Aliabadi, M.D.P. Morales, M. Mozaffari, Synthesis of aqueous ferrofluids of $Zn_xFe_{3-x}O_4$ nanoparticles by citric acid assisted hydrothermal-reduction route for magnetic hyperthermia applications, J. Magn. Magn. Mater. 324 (2012) 2211–2217, https://doi.org/10.1016/j.jmmm.2012.02.034.

[38] S. Mørup, M.F. Hansen, C. Frandsen, Magnetic interactions between nanoparticles, Beilstein J. Nanotechnol. 1 (2010) 182–190, https://doi.org/10.3762/bjnano.1.22.

[39] I.J. Bruvera, M.P. Calatayud, G.F. Goya, Determination of the blocking temperature of magnetic nanoparticles: the good, the bad and the ugly, J. Appl. Phys. 118 (2015) 1–8, https://doi.org/10.1063/1.4935484.

[40] I. Sharifi, H. Shokrollahi, S. Amiri, Ferrite-based magnetic nanofluids used in hyperthermia applications, J. Magn. Magn. Mater. 324 (2012) 903–915, https://doi.org/10.1016/j.jmmm.2011.10.017.

[41] P. De La Presa, Y. Luengo, M. Multigner, R. Costo, M.P. Morales, G. Rivero, A. Hernando, Study of heating efficiency as a function of concentration, size, and applied field in α-Fe_2O_3 nanoparticles, J. Phys. Chem. C. 116 (2012) 25602–25610, https://doi.org/10.1021/jp310771p.

[42] F. Arteaga-Cardona, E. Santillán-Urquiza, U. Pal, M.E. Méndoza-Álvarez, C. Torres-Duarte, G.N. Cherr, P. de la Presa, M. Méndez-Rojas, Unusual variation of blocking temperature in bi-magnetic nanoparticles, J. Magn. Magn. Mater. 441 (2017) 417–423, https://doi.org/10.1016/j.jmmm.2017.06.024.